Transport of electron hopping regulated by geometric configuration of quantum-dot arrays

Bowei Wang[1,2], Zimeng Shang[2,3], and Weihua Han[1,2,3]*
[1]*School of Advanced Interdisciplinary Sciences, University of Chinese Academy of Sciences, Beijing 100049, China*
[2]*Engineering Research Center for Semiconductor Integrated Technology, Institute of Semiconductors, Chinese Academy of Sciences, Beijing 100083, China and*
[3]*Center of Materials Science and Optoelectronics Engineering, University of Chinese Academy of Sciences, Beijing 100049, China*

(Received 18 June 2025; revised manuscript received 5 August 2025)

Dopant-atom quantum dot arrays in silicon-based nanostructures constitute a promising platform for quantum computation, quantum simulation, and related applications. Owing to differences in topology and the presence of long-range Coulomb interactions, arrays with distinct geometrical configurations, such as linear, annular, and grid structures, exhibit markedly different electron transport characteristics. In addition, the hopping transport of electrons can be substantially modified by the tuning of electron tunneling and the phase coherence of wave functions. In this work, we establish a generalized Fermi-Hubbard model for dopant-atom quantum dot arrays in silicon-based nanostructures and investigate the mechanism by which the geometrical configuration of the array regulates electron hopping transport. Taking annular quantum dot arrays as a representative example, we systematically analyze the addition energy spectra and conductance characteristics under different array geometrical configurations and electron hopping modes. The respective roles of the on-site electron Coulomb repulsion, inter-site electron Coulomb repulsion energy, long-range electron-ion Coulomb attraction energy, and quantum dot coupling in determining electron hopping behavior are further clarified. The present work provides a basic theoretical framework for understanding the geometrical regulation of hopping-mediated electron transport in quantum dot arrays.

Keywords: quantum-dot arrays, electron hopping, geometric configurations, generalized Fermi–Hubbard model
PACS: 73.21.La, 71.10.Fd, 71.27.+a **DOI:** 10.7498/aps.74.20250784
CSTR: 32037.14.aps.74.20250784

1. INTRODUCTION

Quantum-dot arrays, as artificial quantum systems, have attracted extensive attention due to their distinctive electronic structures and high tunability, showing great potential in quantum computing, quantum simulation, and nanoelectronics. In recent years, with continuous advances in microscale and nanoscale fabrication, the preparation and manipulation of dopant-atom quantum-dot arrays have achieved significant progress [1, 2]. In silicon, dopant atoms confined in low-dimensional nanoscale local regions can form quantum-dot arrays. Owing to their discrete electronic levels and Coulomb interactions, such arrays provide an ideal platform for investigating strongly correlated electron systems and quantum many-body physics, offering new opportunities for both experimental studies and theoretical explorations.

From the theoretical perspective, the Hubbard model [3] has been widely adopted to describe electron behaviors in quantum-dot arrays [4] because of its simplicity and universality. By incorporating local Coulomb interactions and electron hopping, it can capture key physical phenomena in quantum-dot arrays, such as quantum phase transitions, charge-density waves, and quantum entanglement. However, the conventional Hubbard model lacks an explicit description of geometry-dependent inter-site Coulomb interactions in quantum-dot arrays, and it also does not adequately account for long-range hopping processes. Consequently, it fails to describe electron transport properties of quantum-dot arrays with complex geometries and intricate hopping modes.In practice, both the geometry of the array and the hopping modes can profoundly influence electron transport. Quantum-dot arrays with different geometries, such as linear, annular, and square configurations, exhibit markedly distinct transport behaviors. Linear arrays, due to their simple topology, typically display two symmetric envelopes of conductance peaks [5]. In contrast, annular arrays, featuring periodic boundary conditions, exhibit unique degeneracies and topological properties. Under a magnetic field perpendicular to the ring plane, these degenerate states can be split, yielding a periodic magnetic field response in transport [6]. For more complex two-dimensional quantum-dot arrays, transport becomes even richer: electrons are influenced not only by local Coulomb interactions but also by complex long-range Coulomb interactions. At low filling, such long-range interactions can drive electrons to localize toward the center of the array, thereby suppressing transport [7]. Meanwhile, the hopping modes also play a critical role. Long-range hopping can protect electron coherence and enhance the robustness of transport against disorder [8]. Moreover, in linear arrays, increasing the number of quantum dots in series reduces the height of conductance peaks, whereas increasing the number of dots in parallel increases the peak height [9], highlighting the profound impact of geometric arrangement on quantum transport.

*Corresponding author. E-mail: weihua@semi.ac.cn

The paper is an English translated version of the original Chinese paper published in Acta Physica Sinica. Please cite the paper as: WANG Bowei, SHANG Zimeng, HAN Weihua. Transport of electron hopping regulated by geometric configuration of quantum-dot arrays Acta Phys. Sin., 2025, 74(19): 197301. DOI: 10.7498/aps.74.20250784

In this work, we establish a generalized Fermi-Hubbard framework for dopant-atom quantum-dot arrays in silicon-based nanostructures, with the aim of providing a unified theoretical description of the interplay between array geometry, electron hopping behavior, and quantum transport spectrum. Within this framework, the geometric distribution of quantum dots and the electron hopping modes are parameterized, respectively by an effective Euclidean distance matrix $\boldsymbol{D}$ and an adjacency matrix $\boldsymbol{A}$, thereby enabling an explicit expression of array geometric configuration and electron hopping modes in the Hubbard Hamiltonian. As a representative example, a two-dimensional annular array is considered for the formulation and implementation of the generalized Hubbard model, on the basis of which the corresponding addition-energy and conductance spectra are evaluated to examine the electron transport characteristics of dopant-atom quantum-dot arrays associated with different array geometric configurations and electron hopping modes. It is anticipated that the generalized framework proposed here will provide theoretical support for the design and optimization of dopant-atom quantum-dot arrays and will further establish a foundation for the exploration of silicon-based quantum devices and related quantum technologies.

2. GENERALIZED HUBBARD MODEL CONSTRUCTION METHOD FOR TWO-DIMENSIONAL ARRAYS

2.1. Matrix representation of geometric characteristics of two-dimensional array

Compared with the one-dimensional array, the two-dimensional dopant-atom array structure allows richer regulation of electron quantum transport behavior. Therefore, it is of considerable significance to construct the Fermi-Hubbard model of the two-dimensional dopant-atom array and explore the transport properties of electrons in the array.

For the one-dimensional array, the description of its geometric characteristics is relatively simple, which only need to index dopant atoms sequentially (from one end of the array to the other), and obtain the corresponding coordinate x_i to determine the geometric characteristics of the array. Because the numbering is done in order, the neighboring relationship between dopant atoms can be obtained directly. However, when the dimension of the array rises to two dimensions, sequential indexing alone cannot explicitly encode adjacency relationships between dopant atoms, so that coordinates need to be represented as ordered array (x_i, y_i), leading to additional complexity in describing inter-site relations.In fact, the absolute positions of dopant atoms are non-essential, rather the critical determinant is their relative configuration, characterized by the set of inter-atomic distances. Hence, coordinate-based representations are not optimal. We find that the effective Euclidean distance matrix $\boldsymbol{D}$ can completely and uniquely represent the geometry of a two-dimensional dopant-atom array by determining the distance between dopant atoms, where the effective Euclidean distance matrix $\boldsymbol{D}$ is a matrix of $N \times N$, N is the number of dopant atoms in the array, and the matrix element d_{ij} is used to describe the distance between the dopant atom i and j.

Once the array geometry has been specified, the determination of the electron hopping paths within the array becomes necessary for the characterization of electron transport behavior. Such hopping paths are abstracted as the connectivity among dopant-atom sites, which is described by the adjacency matrix $\boldsymbol{A}$. Specifically, the matrix element a_{ij} of $\boldsymbol{A}$ characterizes the connectivity between sites i and j. When $a_{ij} = 1$, a connection between sites i and j is established, indicating the existence of a hopping path between dopant atoms i and j. By contrast, when $a_{ij} = 0$, no such connection is present between the two sites, and electron hopping between dopant atoms i and j is therefore forbidden.

The adjacency matrix $\boldsymbol{A}$ and the effective Euclidean distance matrix $\boldsymbol{D}$ describe the geometric characteristics of the two-dimensional array and the hopping path of electrons in the array with an algebraic representation, which can most intuitively describe the position relationship of dopant atoms and the hopping behavior of electrons, and also provide convenience for obtaining the Hubbard Hamiltonian matrix and solving its eigenvalues through quantum state operations.

2.2. Extended Hubbard model for two-dimensional arrays

The dopant-atom quantum-dot array is a quantum system with electron correlation effect, and the Hamiltonian of the system is formulated by the second-quantized extended Hubbard Hamiltonian:

$$\begin{aligned}\hat{H} = &\sum_i \varepsilon_i n_i - \sum_{i \neq j} \sum_{\sigma=\uparrow,\downarrow} t_{ij}(c^{\dagger}_{i\sigma} c_{j\sigma} + h.c.) \\ &+ U \sum_i n_{i\uparrow} n_{i\downarrow} + \sum_{i<j} W_{ij} n_i n_j\end{aligned} \tag{1}$$

where ε_i is the on-site energy of an electron when it occupies the dopant atom i, n_i represents the number of electrons on dopant atom i, t_{ij} is the coupling strength of electron tunneling between the dopant atom i and j, σ represents the spin direction of the electron, and $c^{\dagger}_{i\sigma} c_{j\sigma}$ is the creation and annihilation operators; U is the on-site electron repulsion energy, which is the Coulomb repulsion energy of a pair of electrons with opposite spin occupying the same dopant atom, and $n_{i\uparrow}$ and $n_{i\downarrow}$ respectively represents the number of up-spin electrons and down-spin electrons on the dopant atom i; W_{ij} is the inter-site electron repulsion energy, describing the Coulomb repulsion between an electron on dopant atom i and an electron on dopant atom j.

2.2.1. Representation of quantum states and construction of Hamiltonian matrices

To solve the energy eigenvalues of Fermi-Hubbard system, the second-quantized Hubbard Hamiltonian is transformed into the Hamiltonian matrix, and the eigenvalues are solved by the exact diagonalization method. For an N-site Fermi-

Hubbard system, the site occupation numbers are chosen as basis vectors to describe the quantum state in the Hilbert space:

$$|\psi_\alpha\rangle = \left|n_{1\uparrow} n_{2\uparrow} \cdots n_{N\uparrow} n_{1\downarrow} n_{2\downarrow} \cdots n_{N\downarrow}\right\rangle, \tag{2}$$

where $n_{i\sigma}$ is the occupation number of electrons with spin σ on the site i. According to the Pauli exclusion principle, no two electrons with the same spin can be occupied on a site, so $n_{i\sigma}$ is a binary number 0 or 1. The total number of quantum states of the N site system is 2^{2N}, and the dimension of full Hilbert space is 2^{2N}.

Moreover, the basis vectors can be further classified according to the conserved quantities of the system. Full Hilbert space is divided into a series of subspaces, and the Hamiltonian matrix is diagonalized independently in each subspace to reduce the computational complexity of diagonalization. The total spin number of the system is conserved and there is a commutation relation between the system and the Hubbard Hamiltonian:

$$[\hat{H}, n_\uparrow] = [\hat{H}, n_\downarrow] = 0 \tag{3}$$

where $n_\uparrow = \sum_i n_{i\uparrow}$ is the total number of up-spin electrons and $n_\downarrow = \sum_i n_{i\downarrow}$ is the total number of down-spin electrons. According to the commutation relation, the total Hilbert space can be divided into $(N+1)^2$ subspaces according to the number of up-spin electrons and the number of down-spin electrons $(n_\uparrow, n_\downarrow)$.

With the chosen basis vectors $\left\{\left|\psi_\alpha^{n_\uparrow, n_\downarrow}\right\rangle\right\}$ in the subspace $(n_\uparrow, n_\downarrow)$, the matrix elements of the Hamiltonian matrix $H^{n_\uparrow, n_\downarrow}$ are:

$$H_{\alpha\beta} = \left\langle \psi_\alpha^{n_\uparrow, n_\downarrow} \middle| \hat{H}Big | \psi_\beta^{n_\uparrow, n_\downarrow} \right\rangle = \begin{cases} \sum_i \varepsilon_i n_i + U \sum_i n_{i\uparrow} n_{i\downarrow} + \sum_{i<j} W_{ij} n_i n_j, & \alpha = \beta, \\ -\sum_{i\neq j} \sum_{\sigma=\uparrow,\downarrow} t_{ij} \left\langle \psi_\alpha^{n_\uparrow, n_\downarrow} \middle| c_{i\sigma}^\dagger c_{j\sigma} + c_{j\sigma}^\dagger c_{i\sigma} \middle| \psi_\beta^{n_\uparrow, n_\downarrow} \right\rangle, & \alpha \neq \beta. \end{cases} \tag{4}$$

The diagonal element $H_{\alpha\alpha}$ describes the potential energy term, which includes the interaction between the electron and the ion core, as well as the electron-electron correlation effects, and the off-diagonal term $H_{\alpha\beta}$ describes the kinetic energy term, also known as the hopping term, which is generated by the electron hopping.

2.2.2. *Potential term of the Hubbard Hamiltonian matrix*

The diagonal term of the extended Hubbard Hamiltonian matrix is the potential energy term, which can be divided into three terms: the on-site energy term $\sum_i \varepsilon_i n_i$ describes the total electric potential energy between all electrons and all dopant atoms, the on-site electron repulsion energy term $U \sum_i n_{i\uparrow} n_{i\downarrow}$ describes the total on-site Coulomb repulsion energy for all doubly occupied sites, and the inter-site electron repulsion energy term $\sum_{i<j} W_{ij} n_i n_j$ describes the total inter-site electron repulsion of electrons on all different sites.

The on-site energy ε_i includes the Coulomb interaction exerted on an electron at dopant atom i by all dopant atoms in the array:

$$\varepsilon_i = -E_B + \sum\nolimits_{i\neq j} V_{ij}. \tag{5}$$

In the formula, E_B is the binding energy of the dopant atom, in which the binding energy of a phosphorus (P) donor in Si is about 45 meV. V_{ij} is the electron-ion core long-range Coulomb attraction energy, which describes the Coulomb attraction of other ion cores to the electron on dopant atom i:

$$V_{ij} = -V_0 \int \frac{|\psi(\boldsymbol{r} - \boldsymbol{R}_i)|^2}{|\boldsymbol{r} - \boldsymbol{R}_j|} \mathrm{d}\boldsymbol{r}, \tag{6}$$

where $V_0 = e^2/(4\pi\varepsilon_0\varepsilon_\mathrm{Si})$, $\psi(\boldsymbol{r} - \boldsymbol{R}_i)$ is the ground state $1\mathrm{sA}_1$ multi-valley coupled wave functions [10] on the isolated P donor occupying at $\boldsymbol{R}_i$ in the Si lattice, and $\boldsymbol{R}_i$ and $\boldsymbol{R}_j$ are the position vectors of the dopant atom i and the dopant atom j, respectively.

The on-site electron repulsion energy U describes the repulsion between two electrons with opposite spins occupying the same site. In the Si:P system, the on-site electron repulsion energy U is equivalent to the energy difference between the D^0 state and D^- state of the P atom:

$$\begin{aligned} U &= V_0 \int \frac{|\psi(\boldsymbol{r}_1 - \boldsymbol{R}_i)|^2 |\psi(\boldsymbol{r}_2 - \boldsymbol{R}_i)|^2}{|\boldsymbol{r}_1 - \boldsymbol{r}_2|} \mathrm{d}\boldsymbol{r}_1 \mathrm{d}\boldsymbol{r}_2 \\ &= E_B(D^-) - E_B(D^0) = 43.86\,\mathrm{meV}. \end{aligned} \tag{7}$$

The inter-site electron repulsion energy W_{ij} describes the Coulomb repulsion energy between the electron on the dopant atom i and the electron on the dopant atom j:

$$W_{ij} = V_0 \int \frac{|\psi(\boldsymbol{r}_1 - \boldsymbol{R}_i)|^2 |\psi(\boldsymbol{r}_2 - \boldsymbol{R}_j)|^2}{|\boldsymbol{r}_1 - \boldsymbol{r}_2|} \mathrm{d}\boldsymbol{r}_1 \mathrm{d}\boldsymbol{r}_2. \tag{8}$$

Substituting Eq. (5) into the diagonal term of the Hubbard Hamiltonian matrix yields:

$$\begin{aligned} H_{\alpha\alpha} = & -NE_B - \sum_i n_i \left(\sum\nolimits_{i\neq j} V_{ij}\right) \\ & + U \sum_i n_{i\uparrow} n_{i\downarrow} + \sum_{i<j} W_{ij} n_i n_j. \end{aligned} \tag{9}$$

Moreover, the on-site electron repulsion energy term can be rewritten as:

$$U \sum_i n_{i\uparrow} n_{i\downarrow} = \frac{U}{2} \sum_i n_i (n_i - 1). \tag{10}$$

Introducing the description vector $\boldsymbol{n}_\alpha$ of the occupation number basis vector of the $|\psi_\alpha\rangle$ state:

$$\boldsymbol{n}_\alpha = (n_1, n_2, \ldots, n_N) \tag{11}$$

The electron-ion core long-range Coulomb attraction energy matrix $\boldsymbol{V}$ and the inter-site electron repulsion energy matrix $\boldsymbol{W}$ can be expressed as:

$$\boldsymbol{V} = \begin{cases} V_{ij} & i \neq j \\ 0 & i = j \end{cases} \qquad \boldsymbol{W} = \begin{cases} W_{ij} & i \neq j \\ 0 & i = j \end{cases} \tag{12}$$

With Eqs. (10) to (12), Eq. (9) can be rewritten into matrix form as:

$$H_{\alpha\alpha} = -E_B \boldsymbol{n}_\alpha \mathbf{1} + \boldsymbol{n}_\alpha \boldsymbol{V} \mathbf{1} + \frac{U}{2} \boldsymbol{n}_\alpha (\boldsymbol{n}_\alpha{}^{\mathrm{T}} - \mathbf{1}) + \frac{1}{2} \boldsymbol{n}_\alpha \boldsymbol{W} \boldsymbol{n}_\alpha{}^{\mathrm{T}} \tag{13}$$

where $\mathbf{1}$ is an all-one column vector of size $N \times 1$, and the superscript T denotes the transpose of a matrix or vector.

2.2.3. *Hopping term of the Hubbard Hamiltonian matrix*

According to Eq. (2), the occupation number basis vector of a quantum state is expressed as a binary string, which can be written as a row vector $\boldsymbol{N}$ with a length of $2N$ for the convenience of the following matrix operations:

$$\boldsymbol{N} = (n_{1\uparrow}, n_{2\uparrow}, \cdots, n_{N\uparrow}, n_{1\downarrow}, n_{2\downarrow}, \cdots, n_{N\downarrow}) \tag{14}$$

In this representation, a matrix element of 1 represents occupation, and a matrix element of 0 represents unoccupation. The first N site matrix elements describe the occupation of up-spin electrons, and the last N site matrix elements describe the occupation of down-spin electrons.

For an electron with spin σ to hop from site i to site j, two conditions must be satisfied. First, for the hopping process to yield a non-zero result, the initial and final states must satisfy specific occupancy constraints: an electron with spin σ must be present at site i and site j must be vacant. Mathematically, this requires the occupation numbers to be $n_{i\sigma} = 1$ and $n_{j\sigma} = 0$. Secondly, the possibility of electron hopping between sites i and j is intrinsically linked to their geometric connectivity. This condition is encoded in the adjacency matrix $\boldsymbol{A}$, where $a_{ij} = a_{ji} = 1$ indicates that sites i and j are connected.

Before and after the hopping of an electron with spin σ, the initial state $\left|\psi_\alpha^{n_\uparrow, n_\downarrow}\right\rangle$ and the final state $\left|\psi_\beta^{n_\uparrow, n_\downarrow}\right\rangle$ are represented by the vectors $\boldsymbol{N}_\alpha^{\mathrm{I}}$ and $\boldsymbol{N}_\beta^{\mathrm{F}}$, respectively. The two vectors differ only in the entries $n_{i\sigma}$ and $n_{j\sigma}$, which are interchanged in $\boldsymbol{N}_\alpha^{\mathrm{I}}$ to generate $\boldsymbol{N}_\beta^{\mathrm{F}}$. Such an exchange operation can be completed by the permutation matrix $\boldsymbol{P}_{i,j,\sigma}$ of size $2N \times 2N$:

$$\boldsymbol{P}_{i,j,\uparrow} = \begin{pmatrix} \boldsymbol{P}_{i,j} & \boldsymbol{O} \\ \boldsymbol{O} & \boldsymbol{I} \end{pmatrix}, \qquad \boldsymbol{P}_{i,j,\downarrow} = \begin{pmatrix} \boldsymbol{I} & \boldsymbol{O} \\ \boldsymbol{O} & \boldsymbol{P}_{i,j} \end{pmatrix} \tag{15}$$

where $\boldsymbol{P}_{i,j}$ denotes a permutation matrix of order N, obtained by interchanging the i-th and j-th rows of the identity matrix $\boldsymbol{I}$ of order N. Here $\boldsymbol{O}$ is the zero matrix of order N, and $\boldsymbol{I}$ denotes the identity matrix of order N.

The transition process corresponding to the initial state $\left|\psi_\alpha^{n_\uparrow, n_\downarrow}\right\rangle$ and the final state $\left|\psi_\beta^{n_\uparrow, n_\downarrow}\right\rangle$ can be described as

$$\left(\boldsymbol{N}_\beta^{\mathrm{F}}\right)^T = \boldsymbol{P}_{i,j,\sigma} \left(\boldsymbol{N}_\alpha^{\mathrm{I}}\right)^T \tag{16}$$

Meanwhile, the corresponding element $H_{\langle\alpha,\beta\rangle}$ in the Hubbard Hamiltonian matrix satisfies

$$H_{\langle\alpha,\beta\rangle} = -t_{ij} \tag{17}$$

where $\langle\alpha, \beta\rangle$ denotes two quantum states that can be transformed into each other by a single hopping process.

The adjacency matrix $\boldsymbol{A}$ contains all allowed hopping information, and the set of permutation matrices $\{\boldsymbol{P}_{i,j,\sigma}\}$ can be constructed according to all nonzero elements of the adjacency matrix $\boldsymbol{A}$. The final-state set $\left\{\boldsymbol{N}_\beta^{\mathrm{F}}\right\}$, comprising all quantum states reachable from the initial state $\boldsymbol{N}_\alpha^{\mathrm{I}}$ through any permutation matrix $\boldsymbol{P}_{i,j,\sigma} \in \{\boldsymbol{P}_{i,j,\sigma}\}$ (excluding $\boldsymbol{N}_\alpha^{\mathrm{I}}$ itself), represents the complete set of accessible final states $\left\{\left|\psi_\beta^{n_\uparrow, n_\downarrow}\right\rangle\right\}$ corresponding to the initial state $\left|\psi_\alpha^{n_\uparrow, n_\downarrow}\right\rangle$ within the two-dimensional array. Clearly, the final-state set $\left\{\boldsymbol{N}_\beta^{\mathrm{F}}\right\}$ does not contain $\boldsymbol{N}_\alpha^{\mathrm{I}}$. The transition condition implies that an electron with spin σ is allowed to hop between sites i and j only when the occupation numbers $n_{i\sigma}$ and $n_{j\sigma}$ in the initial state $\boldsymbol{N}_\alpha^{\mathrm{I}}$ are different. Specifically, $\boldsymbol{N}_\beta^{\mathrm{F}}$ is obtained by interchanging the entries $n_{i\sigma}$ and $n_{j\sigma}$ in $\boldsymbol{N}_\alpha^{\mathrm{I}}$, and it must therefore differ from $\boldsymbol{N}_\alpha^{\mathrm{I}}$. By traversing all initial states $\boldsymbol{N}_\alpha^{\mathrm{I}}$, the corresponding final-state sets $\left\{\boldsymbol{N}_\beta^{\mathrm{F}}\right\}$ are obtained, thereby establishing the mapping relation between the set $\left\{\boldsymbol{N}^{\mathrm{I}}\right\}$ of all initial states and the set $\left\{\boldsymbol{N}^{\mathrm{F}}\right\}$ of all final states under the action of the permutation-matrix set $\{\boldsymbol{P}_{i,j,\sigma}\}$. The essence of this mathematical mapping is the transition relation between states, on the basis of which all hopping terms $H_{\alpha\beta}$ in the Hubbard Hamiltonian can be constructed.

2.3. Calculation method of electron transport spectrum for two-dimensional array

2.3.1. *Addition energy spectrum of a two-dimensional array*

After constructing the potential-energy term $H_{\alpha\alpha}$ and the hopping term $H_{\alpha\beta}$, the Hubbard Hamiltonian matrix $\boldsymbol{H}^{n_\uparrow, n_\downarrow}$ of the subspace $(n_\uparrow, n_\downarrow)$ can be formed. Diagonalizing the matrix yields a set of many-body energy eigenvalues $E_m^{n_\uparrow, n_\downarrow}$, where m labels the eigenstates in the $(n_\uparrow, n_\downarrow)$ subspace, with $m = 0$ denoting the ground state.Consider a system with a total of n electrons, whose Hilbert space is composed of all subspaces $(n_\uparrow, n_\downarrow)$ satisfying $n_\uparrow + n_\downarrow = n$. The eigenlevel $E_m(n)$ of the n electron system is obtained by collecting all eigenvalues $E_m^{n_\uparrow, n_\downarrow}$ from these subspaces and ordering them by energy, where $E_0(n)$ represents the ground state energy.

Adding an electron from the electrode to the array requires an additional energy cost, referred to as the addition energy.

When the n-th electron is added to the array, the ground state changes from that of the $n-1$ electron system to that of the n electron system. The energy difference between these two ground states is defined as the addition energy of the n-th electron:

$$E_{\mathrm{ad}}(n) = E_0(n) - E_0(n-1) \tag{18}$$

The addition energy measures the cost of inserting an extra electron into a many-body system, and the spacing of the addition-energy spectrum provides direct information about the strength of electron-electron interactions. In strongly correlated systems, the addition energy spectrum can further reveal distinct transport behaviors governed by the competition between the on-site interaction U and the coupling strength t.

2.3.2. *Conductance spectrum of a two-dimensional array*

Based on the tunneling rate, the temperature-dependent linear-response conductance of the two-dimensional array under the low-bias condition ($V_{\mathrm{DS}} \to 0$) can be written as a function of the electrode chemical potential μ [5]:

$$G(\mu) = \frac{\Gamma e^2}{\hbar k_{\mathrm{B}} T} \sum_{n_\sigma, n_{\bar\sigma}} \sum_{\alpha,\beta,\sigma} \frac{M^{(L),n_\sigma,n_{\bar\sigma}}_{\alpha,\beta,\sigma} M^{(R),n_\sigma,n_{\bar\sigma}}_{\alpha,\beta,\sigma}}{M^{(L),n_\sigma,n_{\bar\sigma}}_{\alpha,\beta,\sigma} + M^{(R),n_\sigma,n_{\bar\sigma}}_{\alpha,\beta,\sigma}} \times P^{n_\sigma,n_{\bar\sigma}}_{\alpha} [1 - f_{\mathrm{FD}}(E^{n_\sigma,n_{\bar\sigma}}_{\alpha} - E^{n_\sigma-1,n_{\bar\sigma}}_{\beta} - \mu)], \tag{19}$$

where f_{FD} denotes the Fermi-Dirac distribution function. The transition matrix element $M^{(\mathrm{L}),n_\sigma,n_{\bar\sigma}}_{\alpha,\beta,\sigma}$ represents the probability of a spin σ electron tunneling from the left electrode to the array, causing the array to transition from the $\left|\psi^{n_\sigma-1,n_{\bar\sigma}}_{\beta}\right\rangle$ quantum state in the $(n_\sigma - 1, n_{\bar\sigma})$ subspace to the $\left|\psi^{n_\sigma,n_{\bar\sigma}}_{\alpha}\right\rangle$ quantum state in the $(n_\sigma, n_{\bar\sigma})$ subspace:

$$\begin{cases} M^{(L),n_\sigma,n_{\bar\sigma}}_{\alpha,\beta,\sigma} = \sum_{j\in L} \left| \left\langle \psi^{n_\sigma,n_{\bar\sigma}}_{\alpha} \right| c^{\dagger}_{j\sigma} \left| \psi^{n_\sigma-1,n_{\bar\sigma}}_{\beta} \right\rangle \right|^2, \\ M^{(R),n_\sigma,n_{\bar\sigma}}_{\alpha,\beta,\sigma} = \sum_{j\in R} \left| \left\langle \psi^{n_\sigma,n_{\bar\sigma}}_{\alpha} \right| c^{\dagger}_{j\sigma} \left| \psi^{n_\sigma-1,n_{\bar\sigma}}_{\beta} \right\rangle \right|^2. \end{cases} \tag{20}$$

$\Gamma = 2\pi V^2$ is a constant, and V characterizes the contact barrier between electrodes and the quantum-dot array. For simplicity, the couplings between the array and the left and right electrodes are assumed to be identical. $P^{n_\sigma,n_{\bar\sigma}}_{\alpha}$ denotes the occupation probability of the quantum state $\left|\psi^{n_\sigma,n_{\bar\sigma}}_{\alpha}\right\rangle$:

$$P^{n_\sigma,n_{\bar\sigma}}_{\alpha} = \frac{\exp(-(E^{n_\sigma,n_{\bar\sigma}}_{\alpha} - n\mu)/k_{\mathrm{B}}T)}{\sum_{n_\sigma,n_{\bar\sigma},\alpha} \exp(-(E^{n_\sigma,n_{\bar\sigma}}_{\alpha} - n\mu)/k_{\mathrm{B}}T)} \tag{21}$$

where $E^{n_\sigma,n_{\bar\sigma}}_{\alpha}$ and $E^{n_\sigma-1,n_{\bar\sigma}}_{\beta}$ are the eigenenergies corresponding to the $\left|\psi^{n_\sigma,n_{\bar\sigma}}_{\alpha}\right\rangle$ and the $\left|\psi^{n_\sigma-1,n_{\bar\sigma}}_{\beta}\right\rangle$, respectively.

3. RESULTS

3.1. Representation of geometrical and hopping properties of annular array

To analyze electron transport in a hydrogenic dopant-atom quantum-dot array, we assume that the dopant atoms are periodically arranged in the two-dimensional plane of a silicon nanosheet channel, as shown in Fig. 1, each unit cell exhibits central rotational symmetry, with the dopant atoms distributed on a circle in a regular polygonal configuration, thereby forming an annular array. The silicon nanosheet channel is connected to the source and drain electrodes. In the low-bias limit ($V_{\mathrm{DS}} \to 0$), the chemical potential of electrons on the donor atoms is assumed to be controlled solely by the gate voltage (V_{GS}). To capture the essential transport characteristics of an ordered two-dimensional array, we further assume that electron hopping is confined to a single unit cell and that only the Coulomb interactions within that unit cell are considered. Under these assumptions, the transport problem in a spatially ordered two-dimensional dopant-atom array can be reduced to that in the annular array corresponding to a single unit cell. By analyzing the electron transport in Fermi-Hubbard arrays, the hopping behavior of electrons in strongly correlated systems is explored.

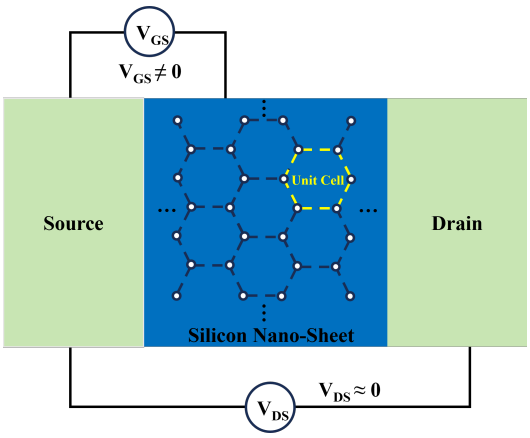

FIG. 1. The schematic structure of silicon-based dopant atom transistor.

The transport properties of electrons in the dopant atom quantum-dot array are primarily determined by the geometry of the array and the electron hopping modes, which can be uniquely characterized by the effective Euclidean distance matrix $\boldsymbol{D}$ and the adjacency matrix $\boldsymbol{A}$.

For an annular array consisting of N sites, the dopant atoms are labeled clockwise from 1 to N in turn, as shown in Fig. 2(a). According to the geometric relationship of the regular polygon, as shown in Fig. 2(b), the inter-dopant separation d_{ij} between the dopant atom i and the dopant atom j is given by:

$$\begin{cases} d = R\sin(\theta/2), \\ d_{ij} = R\sin(\theta_{ij}/2), \\ \theta_{ij} = |i-j|\theta. \end{cases}$$

Upon substituting $\theta = 2\pi/N$, d_{ij} can be written as:

$$d_{ij} = d\csc\frac{\theta}{2}\sin\frac{|i-j|\theta}{2} = d\csc\frac{\pi}{N}\sin\frac{|i-j|\pi}{N}, \quad (22)$$

where d is the side length of a regular polygon, also the nearest-neighbor inter-dopant separation.

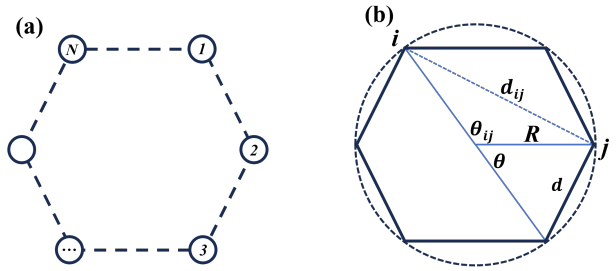

FIG. 2. (a) The distribution of annular array dopant atoms; (b) the geometric relationships of regular polygons.

For an N-site ($N \geq 6$) annular array, three models with distinct electron hopping modes are considered according to different hopping mechanisms: the nearest-neighbor hopping (NNH) model, which only allows electron hopping between nearest-neighbor dopant atoms; the next-nearest-neighbor hopping (NNNH) model, where electrons can hop between both nearest-neighbor and next-nearest-neighbor dopant atoms; and the long-range hopping (LRH) model, where electrons can hop between any two sites. We further constructed the adjacency matrices corresponding to these three hopping modes:

$$\boldsymbol{A}_{\mathrm{NNH}} = \begin{pmatrix} & 1 & & & & & & 1 \\ 1 & & 1 & & & & & \\ & 1 & & 1 & & & & \\ & & 1 & & 1 & & & \\ & & \ddots & & & \ddots & & \\ & & & & 1 & & 1 & \\ & & & & & 1 & & 1 \\ 1 & & & & & & 1 & \end{pmatrix}$$

$$\boldsymbol{A}_{\mathrm{NNNH}} = \begin{pmatrix} & 1 & 1 & & & & 1 & 1 \\ 1 & & 1 & 1 & & & & 1 \\ 1 & 1 & & 1 & 1 & & & \\ & 1 & 1 & & 1 & 1 & & \\ & \ddots & \ddots & & & \ddots & \ddots & \\ & & & 1 & 1 & & 1 & 1 \\ 1 & & & & 1 & 1 & & 1 \\ 1 & 1 & & & & 1 & 1 & \end{pmatrix} \quad (23)$$

$$\boldsymbol{A}_{\mathrm{LRH}} = \begin{pmatrix} & 1 & 1 & 1 & \cdots & 1 & 1 & 1 \\ 1 & & 1 & 1 & \cdots & 1 & 1 & 1 \\ 1 & 1 & & 1 & \cdots & 1 & 1 & 1 \\ 1 & 1 & 1 & & \cdots & 1 & 1 & 1 \\ \vdots & \vdots & \vdots & \vdots & \ddots & 1 & 1 & 1 \\ 1 & 1 & 1 & 1 & 1 & & 1 & 1 \\ 1 & 1 & 1 & 1 & 1 & 1 & & 1 \\ 1 & 1 & 1 & 1 & 1 & 1 & 1 & \end{pmatrix}.$$

3.2. Geometry-dependent energy parameters of annular arrays

In the extended Hubbard model, the energy parameters depend on the geometrical characteristics of the array because they vary with the inter-site spacing. According to the $1sA_1$ multivalley-coupled wave function of the ground state electron bound to the isolated P dopant atom in silicon within the framework of effective-mass theory, the coupling strength t_{ij}, the long-range Coulomb attraction energy V_{ij}, and the inter-site electron repulsion energy W_{ij} can be expressed as a function of inter-dopant separation d_{ij}, as shown in Fig. 3.

The coupling strength t_{ij} exhibits an exponential oscillatory decay with the inter-dopant separation d_{ij}, which can be described as [11]:

$$t_{ij} \approx \frac{2}{1-{S_{ij}}^2}\sum_{\mu=1}^{6}\delta_\mu(\boldsymbol{R}_i-\boldsymbol{R}_j)\cos(\boldsymbol{k}_\mu\cdot(\boldsymbol{R}_i-\boldsymbol{R}_j)) \quad (24)$$

where $\delta_\mu(\boldsymbol{R}_i-\boldsymbol{R}_j)$ is the attenuation factor, which reduces to $\delta_\mu(\boldsymbol{R}_i-\boldsymbol{R}_j) \approx e^{-d_{ij}/a_{\mathrm{B}}}$ in the limit of large d_{ij}, and a_{B} is the Bohr radius of a P donor in Si. The term $\cos\left[\boldsymbol{k}_\mu\cdot(\boldsymbol{R}_i-\boldsymbol{R}_j)\right]$ is responsible for the oscillatory variation of the coupling strength t_{ij}. The blue curves in Fig. 3(b) and Fig. 3(c) describe the dependence of the coupling strength t_{ij} on the inter-dopant separation d_{ij}. As d_{ij} increases, t_{ij} decays approximately exponentially. The red curve marks the peak positions of the blue curve. At these points, d_{ij} is an integer multiple of the Si lattice constant a_{Si}, at which the coupling strength reaches a local maximum and the system energy attains a local minimum. It also provides a plausible explanation for the tendency of phosphorus dopants to preferentially occupy substitutional sites within the Si lattice. When P is an interstitial dopant, the ionized dopant will form a deeper potential well at the interstitial, which leads to the strong localization of the electron wave function, the decrease of orbital overlap and the decrease of coupling strength. By contrast, when P acts as a substitutional dopant, the coupling strength along [100] and [110] directions decreases with the increase of the distance between dopant atoms, which is due to the decrease of the orbital overlap between dopant atoms and the energy difference between bonding and antibonding orbitals, resulting in the decrease of the coupling strength, the decrease of electron delocalization and the increase of electron localization. However, at short dopant separations, the coupling strength along [110] crystal direction exhibits pronounced oscillations, markedly different from that along the [100] crystal direction, due to the interference effect of multi-valley wave function superimposed with periodic oscillation [12, 13], which leads to the emergence of near-zero coupling strengths at specific separations, thereby creating a transport bottleneck. The yellow curve in the figure is the fitted dependence of the coupling strength t_{ij} of the substitutional P atom and inter-dopant separation d_{ij}, revealing an obvious exponential decay behavior of t_{ij} with increasing d_{ij}. The fitted Bohr radius $\widehat{a_{\mathrm{B}}}$ is about 1.9 nm, which is reasonably close to the actual Bohr radius $a_{\mathrm{B}} = 2.5$ nm of P dopants in Si. With increasing inter-dopant separation, the exponential decay behavior becomes increasingly prominent, accompanied by a gradual weakening of the oscillatory behavior. Accordingly,

in the large-separation limit, t_{ij} can be approximated as an exponential function of d_{ij}:

$$t_{ij} \approx t_0 \exp\Big(-\frac{d_{ij}}{a_B}\Big). \tag{25}$$

Substituting the annular-array dopant-atom spacing relation given in Eq. (22) into Eq. (25), we obtain:

$$t_{ij} \approx t_0 \exp\Big(-\frac{d}{a_B}\csc\frac{\pi}{N}\sin\frac{|i-j|\pi}{N}\Big), \tag{26}$$

where t_0 can be determined by fitting the relationship between t_{ij} and d_{ij} in the large-separation limit. For the [100] crystal direction, $t_0 \approx 160\,\mathrm{meV}$; for the [110] direction, $t_0 \approx 90\,\mathrm{meV}$. Under the large-separation limit, the coupling strength t_{ij} becomes very small, and the variation in t_{ij} arising from geometric configuration is negligible. In this case, the coupling strengths between any different dopant pair in the array can be approximately regarded as uniform and represented by an equivalent coupling strength t, which characterizes the approximate coupling strength of the entire system:

$$t_{ij} \approx t_0 \exp\Big(-\frac{d}{a_B}\csc\frac{\pi}{N}\sin\frac{|i-j|\pi}{N}\Big) \approx t_0 \exp\Big(-\frac{d}{a_B}\Big) = t. \tag{27}$$

Both the long-range Coulomb attraction energy V_{ij} and the inter-site electron repulsion energy W_{ij} are approximately inversely proportional to inter-dopant separation d_{ij}, with $|V_{ij}| > |W_{ij}|$. As d_{ij} increases, V_{ij} and W_{ij} become progressively closer and approach the Coulomb interaction between point charges at the large-separation limit. Rewriting Eq. (6) and Eq. (8) in terms of the electrostatic field Green's function $G(\boldsymbol{R})$, we obtain:

$$\begin{cases} V_{ij}(\boldsymbol{R}) = V_0 \displaystyle\int \frac{\psi^2(\boldsymbol{r}-\boldsymbol{R}_i)}{|\boldsymbol{r}-\boldsymbol{R}_j|}\,\mathrm{d}\boldsymbol{r} = [\psi^2 * G](\boldsymbol{R}), \\ W_{ij}(\boldsymbol{R}) = V_0 \displaystyle\iint \frac{|\psi(\boldsymbol{r}_1-\boldsymbol{R}_i)|^2|\psi(\boldsymbol{r}_2-\boldsymbol{R}_j)|^2}{|\boldsymbol{r}_1-\boldsymbol{r}_2|}\,\mathrm{d}\boldsymbol{r}_1\,\mathrm{d}\boldsymbol{r}_2 \\ \qquad\quad = [\psi^2 * V_{ij}](\boldsymbol{R}) = [\psi^2 * \psi^2 * G](\boldsymbol{R}). \end{cases} \tag{28}$$

where "*" denotes convolution, $G(\boldsymbol{R}) = V_0/|\boldsymbol{R}|$ is the electrostatic-field Green's function, and $\boldsymbol{R} = \boldsymbol{R}_i - \boldsymbol{R}_j$. The full-space extension of the wave function distributes the corresponding effective charge density throughout space, which is equivalent to spreading the original charge over different spatial positions. A more spatially dispersed charge distribution results in a lower charge density, which in turn weakens the electric field and reduces the electrostatic potential energy. When the inter-dopant separation d_{ij} is much larger than the characteristic spatial extent of the charge distribution, the charge distribution can be regarded as point-like with respect to the observation point, and the Coulomb interaction correspondingly degenerates to that between point charges. In the hydrogenic dopant system, when inter-dopant separation d_{ij} exceeds several times the Bohr radius a_B, the charge distribution can be treated as point-like.

Therefore, at a large inter-dopant separation (nearest-neighbor inter-dopant separation $d \geq 8\,\mathrm{nm}$), the Coulomb interaction between point charges can be used to approximate the long-range Coulomb attraction energy V_{ij} and the inter-site electron repulsion energy W_{ij}:

$$\begin{aligned} W_{ij} \approx -V_{ij} \approx \frac{V_0}{d_{ij}} &= \frac{V_0}{d}\sin\frac{\pi}{N}\csc\frac{|i-j|\pi}{N} \\ &= W\sin\frac{\pi}{N}\csc\frac{|i-j|\pi}{N} \end{aligned} \tag{29}$$

where $W = V_0/d$ is the inter-site Coulomb repulsion energy between a pair of electrons on nearest-neighbor sites.

3.3. Addition energy spectrum of an annular array

The addition energy spectrum describes the distribution of the energy required to add or remove an electron from a dopant atomic system, which reflects the characteristics of single particle excitation. Two key parameters in this spectrum are the band broadening and the energy gap. The band broadening represents the extent of electron delocalization, a larger band broadening corresponds to stronger delocalization, whereas a smaller band broadening signifies stronger localization. The energy gap represents the Coulomb barrier that must be overcome by an added electron in a strongly correlated system. A larger gap therefore indicates stronger effective Coulomb repulsion and enhanced localization, whereas a smaller gap implies the opposite [9]. In this sense, the band broadening reflects the conducting nature of the system, while the energy gap reflects its insulating character. Their competition provides important insight into correlation effects and quantum order, and characterizes the dynamical behavior of electrons in many-body strongly correlated systems.

For the dopant-atom quantum-dot array, the band broadening and Coulomb gap in the addition energy spectrum are controlled by three energy parameters: the on-site electron repulsion energy U, the coupling strength t, and the nearest-neighbor inter-site electron repulsion energy W. In the following, the effects of three energy parameters on the Coulomb gap and band broadening will be analyzed for annular arrays with and without inter-site electron repulsion.

In the absence of inter-site electron repulsion, the system is characterized only by the on-site electron repulsion U and the coupling strength t. In order to ensure the validity of the approximate relationships in Eq. (27) and Eq. (29), the energy parameters corresponding to $d = 8\,\mathrm{nm}$ are adopted in the simulations, namely, $E_\mathrm{B} = -45.5\,\mathrm{meV}$, $U = 43.86\,\mathrm{meV}$, and $t = 1.34\,\mathrm{meV}$, as shown in Fig. 4. In the interaction-dominated system ($U \gg t$), the band broadening is only related to the coupling strength and increases with the increase of the coupling strength. For a fixed t, the band broadening of the NNH, NNNH and LRH hopping models increases in turn.

In order to explain the behavior, the tight-binding approximation is employed to estimate the band broadening [14] caused by the coupling strength: $\Delta_t = 2\sum z_i t_i$, where z_i represents the coordination number of the i-th nearest-neighbor dopant atoms. Specifically, $i = 1$ represents the nearest neighbor, $i = 2$ represents the next nearest neighbor, and so on. The quantity t_i represents the coupling strength between the dopant atom and its i-th nearest-neighbor dopant atoms. In the

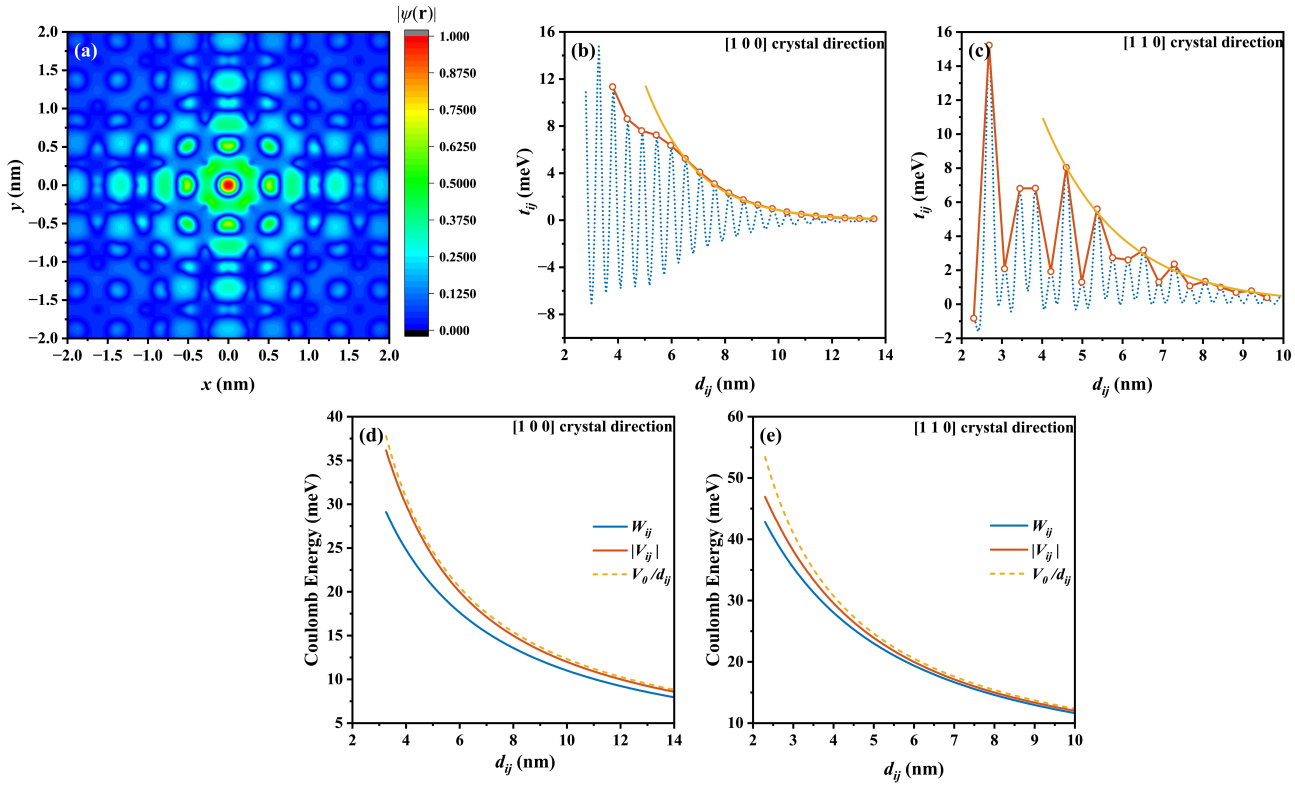

FIG. 3. (a) The ground state $1sA_1$ multi-valley coupled wavefunction of the electron bound to isolated P donor atoms in silicon; (b) the relationship between the coupling strength t_{ij} of dopant atoms arranged along the [100] crystal direction and the distance d_{ij} between dopant atoms; (c) the relationship between the coupling strength t_{ij} of dopant atoms arranged along the [110] crystal direction and the distance d_{ij} between dopant atoms; (d) the relationship between the long-range Coulomb attraction energy V_{ij}, the inter-site electron repulsion energy W_{ij}, and the distance d_{ij} between impurity atoms arranged along the [100] crystal direction; (e) the relationship between the long-range Coulomb attraction energy V_{ij}, the inter-site electron repulsion energy W_{ij}, and the distance d_{ij} between impurity atoms arranged along the [110] crystal direction.

interaction-dominated system, the coupling strength between dopant atoms is treated as approximately uniform and represented by t, and the band broadening is further simplified as:

$$\Delta_t = \left(2\sum z_i\right)\cdot t \tag{30}$$

Therefore, the coupling-induced band broadening has a linear dependence on the coupling strength t, and the corresponding proportionality coefficient is $2\sum z_i$, which is equal to twice the number of hopping paths (the number of sites that electrons can hop to). For NNH, NNNH and LRH hopping models, the number of hopping paths are 2, 4 and $N-1$, respectively. Specifically, in a 6-site annular array, the number of hopping paths is 2, 4, 5, leading to band broadenings of $\Delta_t^{\mathrm{NNH}} = 5.36\,\mathrm{meV}$, $\Delta_t^{\mathrm{NNNH}} = 10.72\,\mathrm{meV}$, $\Delta_t^{\mathrm{LRH}} = 13.4\,\mathrm{meV}$ within the tight binding approximation, while the exact results are $\Delta_t^{\mathrm{NNH}} = 5.22\,\mathrm{meV}$, $\Delta_t^{\mathrm{NNNH}} = 10.81\,\mathrm{meV}$, $\Delta_t^{\mathrm{LRH}} = 13.65\,\mathrm{meV}$. The difference between approximate results and exact results is less than 5%, which proves that the band broadening is proportional to the number of hopping paths in the interaction-dominated system, thereby leading to an increasing band broadenings from the NNH model, the NNNH model to the LRH model. The band broadening Δ_t can also be expanded to the first order in t as:

$$\begin{aligned}\Delta_t &\approx \left.\frac{\partial \Delta_t}{\partial t}\right|_{t=0}\cdot t = \left.\frac{\partial(E_{\mathrm{ad}}(2N)-E_{\mathrm{ad}}(N))}{\partial t}\right|_{t=0}\cdot t \\ &\approx 2\left.\frac{\partial(E_{\mathrm{ad}}(2N))}{\partial t}\right|_{t=0}\cdot t\end{aligned} \tag{31}$$

By comparing Eq. (30) with Eq. (31), one obtains:

$$\left.\frac{\partial(E_{\mathrm{ad}}(2N))}{\partial t}\right|_{t=0} = \sum z_i$$

Namely, the slope of the highest addition energy level at $t = 0$ is equal to the number of hopping paths. As illustrated in Fig. 4(a)–(c), the slopes for NNH, NNNH and LRH models are approximately 2, 4, and 5, respectively, which confirms the validity of the approximation.

The magnitude of the Coulomb gap is determined jointly by the on-site electron repulsion energy U and the coupling strength t, and constitutes a direct measure of the localization tendency of the system. An increase in U gives rise to an enlargement of the Coulomb gap, consequently to an enhancement of electron localization, whereas an increase in t produces a reduction of the Coulomb gap, correspondingly an

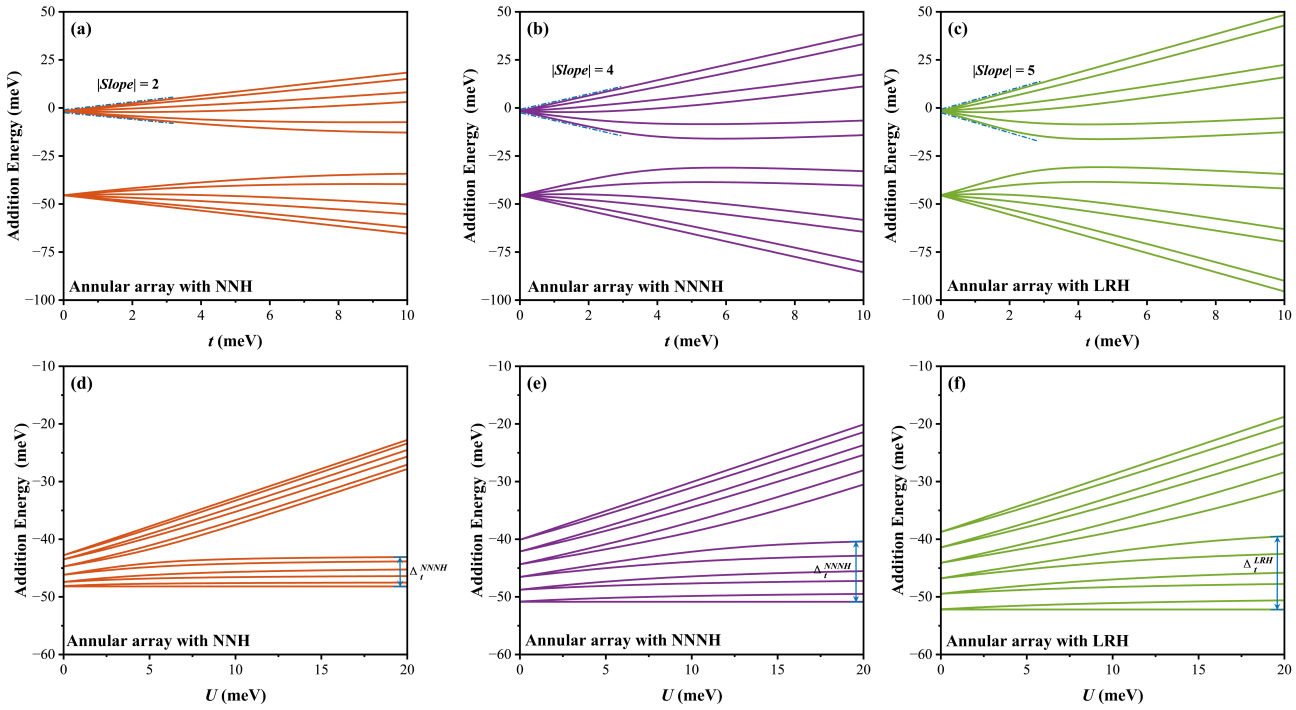

FIG. 4. Addition-energy spectra of a six-site annular array, where red, purple, and green correspond to the NNH, NNNH, and LRH models, respectively: (a)–(c) influence of the coupling strength t on the addition-energy spectra of the array ($U = 43.86$ meV); (d)–(f) influence of the nearest-neighbor inter-site electron repulsion energy W on the addition-energy spectra of the array ($t = 1.34$ meV).

enhancement of electron delocalization. For the purpose of a quantitative characterization of the apparent Coulomb-gap magnitude under the competition between U and t, an effective Coulomb gap U_{eff} is introduced, which is used to be estimated as the difference [15] between the on-site electron repulsion energy U and the band broading Δ:

$$U_{\text{eff}} \approx U - \Delta = U - \left(2\sum z_i\right) \cdot t \tag{32}$$

For the NNH, NNNH, and LRH models, the successive increase in the number of available hopping channels leads to a corresponding successive reduction of the Coulomb gap and an accompanying enhancement of delocalization according to Eq. (32), a trend that is fully consistent with the underlying assumptions of the three hopping models. Within the Fermi-Hubbard system, the competition between the U and the t underlies the occurrence of a transition between a metallic state and a Mott-insulating state, the decisive quantity for such a transition being the sign of the effective Coulomb gap U_{eff}. A positive value of U_{eff} corresponds to the persistence of a Mott-insulating state, whereas a negative value signifies the emergence of metallic behavior [16]. On the basis of the approximate relation in Eq. (32), together with the condition $U_{\text{eff}} = 0$, a qualitative estimate of the critical ratio U/t associated with the change in the transport character of the different hopping models is obtained:

$$(U/t)_{\text{crit}} \approx 2\sum z_i \tag{33}$$

Accordingly, a system possessing a larger number of hopping paths requires a larger on-site repulsion energy in order to maintain localization and therefore exhibits a stronger intrinsic tendency toward delocalization, whereas a system with fewer hopping paths requires a comparatively larger coupling strength for the onset of delocalization and consequently exhibits a stronger tendency toward localization.

In the presence of on-site electron repulsion, modifications arise in both the effective Coulomb gap U_{eff} and the energy band broadening Δ. The influence of inter-site electron repulsion energy on the addition spectrum is examined for the NNH, NNNH, and LRH models, as shown in Fig. 5. The results indicate that the Coulomb gap undergoes an initial stage of near invariance, followed by a subsequent increase with increasing nearest-neighbor inter-site electron repulsion W, accompanied by the formation of a secondary gap. The physical origin of this behavior lies in the rearrangement of electron occupations induced by the combined action of the on-site electron repulsion energy U and the inter-site electron repulsive energy W_{ij}.

In an array dominated by the on-site electron repulsion energy U, energetic minimization gives rise to a pronounced tendency toward single occupancy, such that electrons preferentially distribute over as many distinct sites as possible in order to avoid any additional on-site electron Coulomb repulsion energy cost. Within such a singly occupied configuration, the occupied dopant atom together with its bound electron may be regarded as an effectively neutral entity, with the consequence that the Coulomb interaction between this neutralized site and the remaining electrons vanishes; equivalently, the inter-site electron repulsion energy W_{ij} and the long-range Coulomb attraction energy V_{ij} are mutually cancelled [7]. In a nearly half-

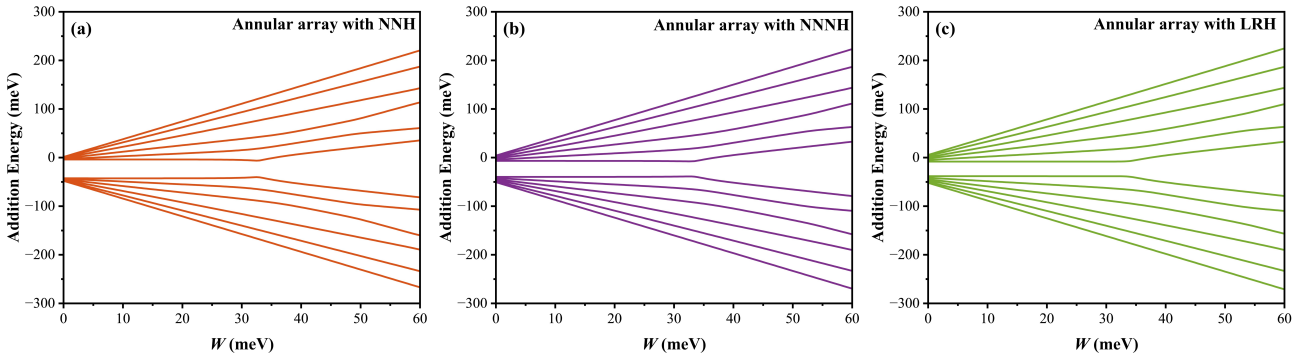

FIG. 5. Modulation effect of the nearest-neighbor inter-site electron repulsion energy W on the addition-energy spectrum of a six-site annular array: (a) NNH model; (b) NNNH model; (c) LRH model.

filled array within the U-dominated regime, the electron number is smaller than the number of sites by one, so that all electrons remain singly occupied and only a single charged dopant site persists in the system. Upon the addition of one electron to such a configuration, a balance is established between the inter-site electron repulsion between the added electron and the pre-existing electrons and the long-range Coulomb attraction between the added electron and the remaining dopant ionic cores, with the result that $E_{\mathrm{ad}}(N)$ remains independent of W. An analogous argument applies to the half-filled array with the electron number equal to the number of sites, for which the addition energy $E_{\mathrm{ad}}(N+1)$ likewise exhibits no dependence on the inter-site electron repulsion. Consequently, the Coulomb gap, defined as the difference between the two addition energies, $E_{\mathrm{ad}}(N+1) - E_{\mathrm{ad}}(N)$ also remains invariant with respect to variations in the inter-site electron repulsion.

In the array dominated by the inter-site electron repulsion energy W_{ij}, the Coulomb gap undergoes a pronounced expansion with increasing W, accompanied by the emergence of a band structure comprising multiple subbands. The physical origin of this behavior lies in a reconstruction of the electronic occupation pattern at sufficiently large W, under which Coulomb repulsion energy cost associated with inter-site electrons exceeds that arising from on-site electrons, thereby rendering a double-occupancy filling pattern energetically favorable as a means of avoiding the larger inter-site repulsive energy cost. Under such circumstances, the ionized dopants and electrons can no longer be regarded as forming effectively neutral entities, with the consequence that the addition energy acquires an explicit dependence on the inter-site electron repulsion and the Coulomb gap correspondingly increases with W. Accordingly, under the competition between the inter-site electron repulsion energy W_{ij} and the on-site electron repulsion energy U, the existence of a critical ratio $\alpha = U/W$ associated with a reconstruction of the electronic configuration is expected. This critical point is defined by the energetic equivalence between the full-sites single-occupancy configuration and the inter-site double-occupancy configuration, such that the equilibrium occupation pattern differs on the two sides of the critical point. The determination of the critical ratio α therefore requires an explicit evaluation of the energies of these two occupation configurations. Under the assumption of a half-filled array containing N dopant atoms and N electrons, together with negligibly small coupling between dopant atoms, the energy E_1 of the inter-site double-occupancy configuration and the energy E_2 of the full-lattice single-occupancy configuration may be written as:

$$\begin{cases} E_1 = -E_B \boldsymbol{n}_1 \mathbf{1} + \boldsymbol{n}_1 \boldsymbol{V} \mathbf{1} + \dfrac{U}{2} \boldsymbol{n}_1 (\boldsymbol{n}_1{}^{\mathrm{T}} - \mathbf{1}) + \dfrac{1}{2} \boldsymbol{n}_1 \boldsymbol{W} \boldsymbol{n}_1{}^{\mathrm{T}}, \\ E_2 = -E_B \boldsymbol{n}_2 \mathbf{1} + \boldsymbol{n}_2 \boldsymbol{V} \mathbf{1} + \dfrac{1}{2} \boldsymbol{n}_2 \boldsymbol{W} \boldsymbol{n}_2{}^{\mathrm{T}}. \end{cases} \tag{34}$$

where $\boldsymbol{n}_1$ denotes the occupation pattern of interval double occupancy, with $\boldsymbol{n}_1 = (2,0,2,0,\ldots)$ for even N, whereas for odd N, $\boldsymbol{n}_1 = (1,2,0,2,0,\ldots)$. The configuration $\boldsymbol{n}_2 = (1,1,1,\ldots)$ represents the occupation mode of full-site single occupancy. Under the condition $E_1 = E_2$, the critical point α can be obtained as:

$$\alpha = \frac{U}{W} = \frac{2(\boldsymbol{n}_2 - \boldsymbol{n}_1)\boldsymbol{V}\mathbf{1} + \boldsymbol{n}_2 \boldsymbol{W} \boldsymbol{n}_2{}^{\mathrm{T}} - \boldsymbol{n}_1 \boldsymbol{W} \boldsymbol{n}_1{}^{\mathrm{T}}}{W \boldsymbol{n}_1 (\boldsymbol{n}_1{}^{\mathrm{T}} - \mathbf{1})} \tag{35}$$

On the basis of the above relation, the critical value α associated with the reconstruction of the electron arrangement in an N-site system is calculated, as shown in Fig. 6. The results indicate the existence of only a single critical point irrespective of the parity of the number of sites, together with a monotonic increase of this critical point with increasing sites. Owing to the difference in electron arrangement between systems with odd and even numbers of sites, the electron arrangement reconstruction critical α exhibits an oscillatory increase with the number of sites and eventually converges to a constant value. By substituting the expressions of $\boldsymbol{n}_2$ and $\boldsymbol{n}_1$ into Eq. (35) and performing an approximation, one obtains:

$$\begin{cases} \alpha = \dfrac{\boldsymbol{n}_2 \boldsymbol{W} \boldsymbol{n}_2^{\mathrm{T}} - \boldsymbol{n}_1 \boldsymbol{W} \boldsymbol{n}_1^{\mathrm{T}}}{2 \cdot W \cdot N/2} \approx \dfrac{\boldsymbol{n}_2 \boldsymbol{W} \boldsymbol{n}_2^{\mathrm{T}} - \boldsymbol{n}_1 \boldsymbol{W} \boldsymbol{n}_1^{\mathrm{T}}}{NW}, \\ \boldsymbol{n}_2 \boldsymbol{W} \boldsymbol{n}_2^{\mathrm{T}} \approx 2W \displaystyle\sum_{k=1}^{N-1} \left(\frac{N}{k} - 1 \right) = 2WN \left(\ln N + \gamma - 1 \right), \\ \boldsymbol{n}_1 \boldsymbol{W} \boldsymbol{n}_1^{\mathrm{T}} \approx 4W \displaystyle\sum_{k=1}^{N/2-1} \left(\frac{N}{k} - 1 \right) = 2WN \left[\ln (N/2) + \gamma - 1 \right]. \end{cases}$$

The limit value of the critical point $\alpha_{\rm lim}$ is obtained as:

$$\begin{aligned}&\alpha_{\rm lim} = U/W\\ &\approx \frac{2WN(\ln N+\gamma-1)-2WN(\ln[N/2]+\gamma-1)}{NW}\\ &= 2\ln 2 \approx 1.386\end{aligned} \tag{36}$$

The numerical value of the critical point obtained from this analytical treatment is consistent with the simulation results shown in Fig. 6, thereby providing support for the validity of the calculation. For the case $N = 6$, the critical point is found to be $\alpha = 1.345$, with the corresponding critical nearest-neighbor inter-site electron-repulsion energy $W_{\rm crit} = 32.6\,$meV, which is very close to the value at which the Coulomb gap begins to expand in Fig. 5. This correspondence indicates that the enhancement of the Coulomb gap under stronger inter-site electron repulsion originates from the reconstruction of the electron arrangement.

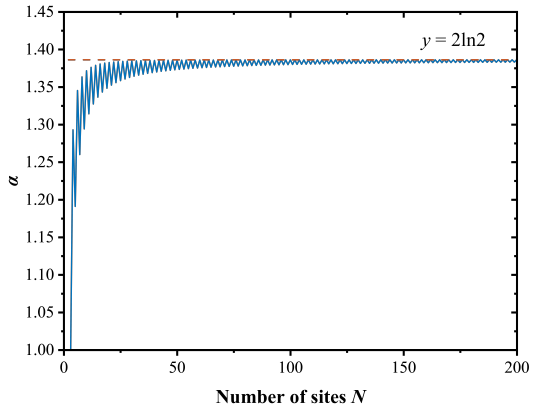

FIG. 6. Relationship between the criticality index α of electronic-configuration reconstruction and the site number N.

In the presence of inter-site electron repulsion and long-range Coulomb attraction, an additional broadening contribution Δ_W arises in the addition energy spectrum. Under the condition $W < W_{\rm crit}$, the additional broadening exhibits a linear dependence on the nearest-neighbor inter-site electron repulsion energy W, from which the total band broadening may be written as:

$$\Delta = \Delta_t + \Delta_W = \left(2\sum z_i\right)\cdot t + \beta W \tag{37}$$

where β denotes the ratio of the band broadening induced by inter-site electron repulsion to the nearest-neighbor inter-site electron repulsion energy, and is hereafter referred to as the correlation broadening coefficient. By definition, the total band broadening may also be expressed as:

$$\Delta = E_{\rm ad}(2N) - E_{\rm ad}(N+1) = E_{\rm ad}(N) - E_{\rm ad}(1). \tag{38}$$

By combining Eq. (37) and Eq. (38), the correlation broadening coefficient β is obtained as:

$$\beta = \frac{\partial \Delta}{\partial W} = \frac{\partial(E_{\rm ad}(2N) - E_{\rm ad}(N+1))}{\partial W}.$$

Since $E_{\rm ad}\,(N+1)$ remains independent of W below the critical value $W_{\rm crit}$, one obtains:

$$\beta = \frac{\partial \Delta}{\partial W} = \frac{\partial(E_{\rm ad}(2N))}{\partial W} \tag{39}$$

where $E_{\rm ad}\,(2N)$ denotes the addition energy associated with the last electron added to the array. In the limit of very small coupling strength t, the electrons are approximately fully localized, with the consequence that the system adopts a unique electron configuration determined by the principle of minimum energy. Under this condition, the last added electron involves the overcoming of the inter-site Coulomb repulsion generated by electrons occupying the other $N-1$ fully occupied sites, the long-range Coulomb attraction associated with the $N-1$ dopant atoms, and the on-site electron repulsion arising from electrons occupying the same site:

$$\begin{aligned}E_{\rm ad}(2N) &= U + 2\sum_{i=1}^{N-1} W_{iN} + \sum_{i=1}^{N-1} V_{iN}\\ &= U + W\sum_{k=1}^{N-1}\sin\frac{\pi}{N}\csc\frac{k\pi}{N}\end{aligned} \tag{40}$$

By the simultaneous solution of Eqs. (37), (39), and (40), the correlation broadening coefficient β and the total band broadening Δ are obtained in the form:

$$\begin{cases}\beta = \displaystyle\sum_{k=1}^{N-1}\sin\frac{\pi}{N}\csc\frac{k\pi}{N},\\ \Delta = \left(2\displaystyle\sum_i z_i\right)t + \left(\sum_{k=1}^{N-1}\sin\frac{\pi}{N}\csc\frac{k\pi}{N}\right)W.\end{cases} \tag{41}$$

It follows that the correlation broadening coefficient β depends solely on the geometric factor. For a six-site annular array, the corresponding value $\beta \approx 3.654$ is found to be consistent with the slope of the addition energy as a function of W in Fig. 5. In the limit of large N, the following approximations become applicable:

$$\begin{cases}\sin(\pi/N) \approx (\pi/N),\\ \displaystyle\sum_{k=1}^{N-1}\csc\frac{k\pi}{N} \approx 2\frac{N}{\pi}\left(\ln\frac{2N}{\pi}+\gamma\right).\end{cases} \tag{42}$$

where $\gamma = 0.5772156649$ is the Euler constant. Substitution of Eq. (42) into Eq. (41) yields an approximately logarithmic dependence of β on N for a sufficiently large N:

$$\beta \approx 2\left(\ln\frac{2N}{\pi}+\gamma\right) \tag{43}$$

Fig. 7 presents the dependence of the correlation broadening coefficient β on the site number N, together with the corresponding logarithmic approximation. The results indicate that the deviation between the value of β estimated from the logarithmic expression in Eq. (43) and the exact value obtained from Eq. (41) remains small, and the accuracy of the logarithmic approximation improves with increasing N. For multi-site annular arrays, this relation therefore provides a convenient estimate of the band broadening induced by inter-site electron repulsion.

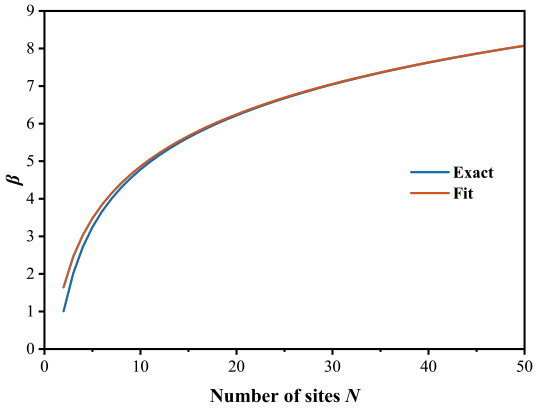

FIG. 7. Relationship between the correlation broadening coefficient β and the number of sites N in an annular array.

3.4. Quantum conductance of an annular array

The quantum conductance of the dopant-atom array arises from electron hopping or tunneling processes, both its magnitude and its spectral distribution exhibit a pronounced dependence on the geometric characteristics of the array as well as on temperature. The geometric characteristics of the dopant-atom quantum-dot array directly govern the relative magnitudes of the inter-site electron repulsion energy W and the coupling strength t through their modulation of the magnitude and spatial distribution of the Coulomb potential, thereby altering the degree of electron localization within the system and consequently inducing a transformation of the transport behavior between hopping-dominated conduction and tunneling-dominated conduction. Such a transport behavior transition is encoded in the structural features of the addition energy spectrum of the coupled quantum-dot array, together with the distribution of peak positions and peak intensities in the quantum-conductance spectrum. Moreover, temperature exerts a direct influence on the electronic energy distribution, thereby giving rise to corresponding modifications in the mode of electron transport. In this section, through an analysis and comparison of the temperature-dependent conductance characteristics of linear and annular arrays composed of dopant atom quantum dots with different geometric characteristics, we examine the effects of the energy parameters, array geometry, distinct electron hopping modes, including nearest-neighbor hopping (NNH), next-nearest-neighbor hopping (NNNH), and long-range hopping (LRH), as well as temperature, on electron transport. The simulation is carried out at very low temperature $T = 2.3\,\mathrm{K}$, with the energy parameters taken from the case corresponding to nearest-neighbor inter-dopant separation $d = 8\,\mathrm{nm}$. By varying a single energy parameter, the effect of the energy parameter on the conductance characteristics of the linear array and the annular array is explored, as shown in Fig. 8. In order to ensure the negligibility of the energy level broadening induced by resonant tunneling, the tunneling rate $\Gamma = 1\,\mu\mathrm{eV}$ is assumed to be much smaller than the distance ΔE_{ad} between adjacent energy levels of the same sub-band in the addition energy:

$$\Delta E_{\mathrm{ad}} = E_{\mathrm{ad}}(n+1) - E_{\mathrm{ad}}(n), \qquad n \neq N$$

where n is the number of electrons in the array, and N is the number of sites. At very low temperatures, the broadening of the conductance peak due to temperature is very small, and the linewidth of the corresponding curve along the x axis is δ, which can be estimated by the full width at half maximum (FWHM) of the conductance peak [17]:

$$\delta \approx 2 \times \mathrm{FWHM} = 2 \times 3.52 k_{\mathrm{B}} T \approx 1.4\,\mathrm{meV} \tag{44}$$

It is evident that the half-peak width is determined solely by temperature, while variations in the energy parameters produce no appreciable alteration in the half-width of the conductance peaks, thereby demonstrating that the linewidths of the curves in Fig. 8 remain essentially invariant under changes in the energy parameters. Moreover, under low-temperature conditions, the peak positions of the sub-peaks remain consistently aligned with the addition energies of the array [18], as demonstrated by comparison between the highlighted curves in Fig. 8 and the addition energy spectra presented in Fig. 4 and Fig. 5. This behavior is attributable to the fact that, at low temperature, the electrons in the quantum-dot array are restricted to occupation of the ground state, such that the incorporation of an additional electron into the array gives rise to a transition from the ground state of the n-electron system to that of the $(n+1)$-electron system, while the corresponding increase in the system energy is compensated by the chemical potential of the $(n+1)$-th electron. Consequently, the chemical potential μ_{n+1} associated with the entry of the $(n+1)$-th electron into the array is identical to the addition energy of the $(n+1)$-th electron in the array:

$$\mu_{n+1} = E_0(n+1) - E_0(n) = E_{\mathrm{ad}}(n+1) \tag{45}$$

The spatial distribution of dopant-atom quantum dots also exerts a pronounced influence on the quantum conductance [19], primarily in two respects. On the one hand, the geometry of the array affects the extent of electron wave-function delocalization within the quantum dots, thereby resulting in differences in the heights of the conductance sub-peaks. As can be inferred from the color mapping along the curves shown in Fig. 8(a) and (e), the conductance of the sub-peaks located at the edges of the upper and lower Hubbard bands in the linear array is substantially smaller than that near the band center, whereas the corresponding variation in the annular array is much less pronounced. This behavior is attributable to the presence of the open-boundary configuration of the linear array, whereby wave-function decay occurs at the edges, resulting in the formation of edge states. Under low-filling conditions, electrons preferentially occupy the central sites of the array [7], under which circumstance electron hopping to the electrodes is correspondingly impeded, thereby resulting in a relatively weak conductance-peak intensity. With increasing electron number in the array, occupation of the edge sites gradually emerges, and the probability of electron tunneling to the electrodes correspondingly increases. Once the electron number exceeds the number of sites, the lower Hubbard band becomes filled, whereupon electrons in the upper Hubbard band

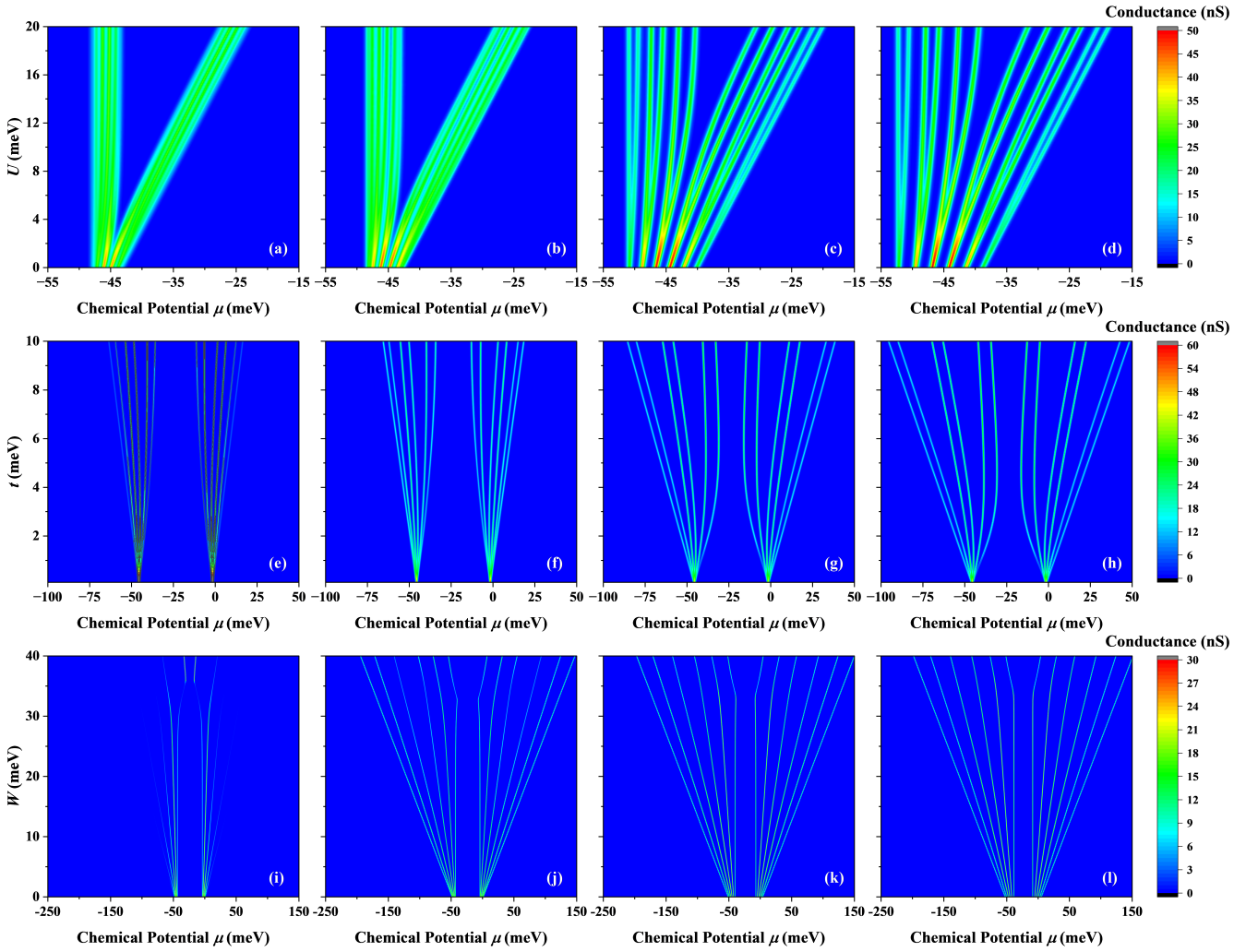

FIG. 8. Response of conductance characteristics to energy parameters in dopant-atom arrays: (a)–(d) influence of the coupling strength t on conductance; (e)–(h) influence of the on-site electron repulsion energy U on conductance; (i)–(l) influence of the nearest-neighbor inter-site electron repulsion energy W on conductance; (a), (e), and (i) one-dimensional array with only nearest-neighbor hopping; (b), (f), and (j) NNH annular array; (c), (g), and (k) NNNH annular array; (d), (h), and (l) LRH annular array.

begin to participate in transport, thereby giving rise to two symmetric bell-shaped conductance envelopes. By contrast, owing to the periodic boundary conditions of the annular array, forward and backward propagating electrons form standing-wave states without the formation of edge states, such that the occupation probability at each site remains approximately uniform and the corresponding variation in conductance peak height is significantly weaker than that in the linear array. As illustrated in Fig. 8(b)–(d) and Fig. 8(f)–(h), although the annular array likewise exhibits two conductance envelopes associated with the upper and lower Hubbard bands, the overall conductance distribution is markedly more homogeneous. Relative to the linear array, the annular array exhibits more clearly defined edge features in the conductance curve, with higher conductance of the edge sub-peaks. On the other hand, the array geometry also strongly affects the inter-site electron-repulsion energy, which modifies the tunneling process through the spatial correlation effect among electrons, and thereby further remodulate both the height and the position of the conductance peaks. Fig. 8(i)–(l) shows that the influence of the inter-site electron repulsion energy is markedly stronger in the one-dimensional array than in the annular two-dimensional array. As the inter-site electron repulsion energy increases, the contrast between the curves and the background is progressively reduced, most prominently at the band edges where transport is strongly suppressed, while the corresponding effect in the two-dimensional array remains negligible. This difference originates from the fact that, in the one-dimensional array, electron motion is confined to a single direction, such that the inter-site Coulomb repulsion is fully aligned with the transport direction, thereby maximally suppressing carrier transport and directly reshaping both the electron configuration and the transport dynamics, as evidenced by the sharp reduction in conductance and the pronounced redistribution relative to the case without inter-

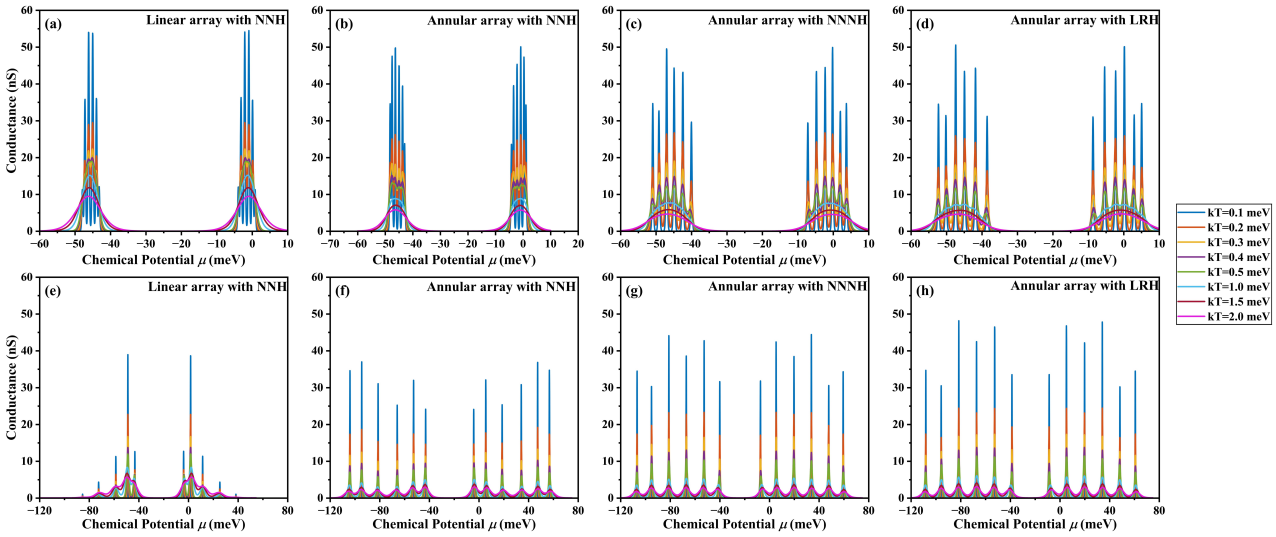

FIG. 9. Temperature-dependent conductance characteristics of dopant-atom arrays: (a)–(d) systems without inter-site repulsion W_{ij} and long-range attraction V_{ij}; (e)–(h) systems with inter-site repulsion W_{ij} and long-range attraction V_{ij}; (a) and (e) one-dimensional array with only nearest-neighbor hopping; (b) and (f) NNH annular array; (c) and (g) NNNH annular array; (d) and (h) LRH annular array.

site electron repulsion. By contrast, in the annular array, electron transport can proceed along multiple directions, such that the direction of the inter-site Coulomb repulsion is not fully aligned with the transport direction, thereby allowing electrons to propagate preferentially along paths subject to weaker inter-site repulsion. Consequently, the suppressive effect of the inter-site electron-repulsion energy on two-dimensional transport is substantially reduced. Moreover, as the number of available hopping paths increases, the directionality of electron transport becomes progressively more complex, further weakening the suppressive effect of the inter-site electron-repulsion energy on electron transport. The influence of the hopping mode on the conductance spectrum is manifested primarily through the number of available hopping paths, with a larger number of hopping paths giving rise to a higher average conductance. According to Eq. (17), an increase in the number of hopping paths leads to an increase in the number of corresponding connected site pairs $\{i, j\}$, and hence to an increase in the number of pairs of many-body states $\langle\alpha, \beta\rangle$ that can be connected through an allowed hopping process. Since the quantum conductance is determined by the transition matrix elements $M^{(L),n_\sigma,n_{\bar{\sigma}}}_{\alpha,\beta,\sigma}$ and $M^{(R),n_\sigma,n_{\bar{\sigma}}}_{\alpha,\beta,\sigma}$ which are nonzero only for hopping-allowed pairs of many-body states $\langle\alpha, \beta\rangle$ as indicated in Eq. (20), an increase in the number of available hopping paths generally enlarges the quantity of hopping-allowed state pairs $\langle\alpha, \beta\rangle$ and hence the number of nonzero transition matrix elements, thereby generating a higher average quantum conductance.

This tendency can be clearly identified in Fig. 8, where the progressively enhanced contrast between the curves of the NNH, NNNH, and LRH models and the background reflects a corresponding increase in the overall conductance level. Since the essential distinction among NNH, NNNH and LRH models resides in the number of hopping paths, the variation in average conductance is attributable primarily to differences in the number of hopping paths. However, an increase in the average conductance does not imply a monotonic increase in the corresponding conductance peak heights of the NNH, NNNH, and LRH models. As shown in Fig. 8, the NNH model exhibits higher sub-peak conductance at the band center than the other models, which is more obvious in Fig. 9. The origin of this behavior lies in the fact that the hopping modes affect not only the number of available transport paths, but also the distribution of electron hopping probability among them, thereby modulating the magnitude of the conductance. In essence, the hopping mode defines the coupling relation among dopant atoms, such that electron hopping is allowed only between mutually coupled sites. Consequently, the probability for electrons to reach the electrodes through different hopping paths is distinct. With an increase in the number of hopping paths, the transport routes by which electrons arrive at the electrodes become progressively more complex, resulting in a further re-modulation of the conductance-peak magnitude. As a result, the conductance distributions associated with different hopping modes in Fig. 8 exhibit pronounced differences. Even for the same array geometry, the conductance envelope shapes associated with different hopping modes remain clearly different, which can be attributed to the redistribution of hopping probabilities induced by the increase of hopping paths.

In order to investigate the influence of temperature on the conductance characteristics of the array, the energy parameters corresponding to a nearest-neighbor inter-dopant separation of $d = 8$ nm are adopted to examine the temperature-dependent conductance behavior of the linear array under NNH mode, together with that of the annular array under three distinct hopping modes, as presented in Fig. 9, with the tunneling rate assumed to be $\Gamma = 1$ μeV.

As shown in Fig. 9, increasing temperature leads to a gradual suppression of the conductance-peak height and a concurrent broadening of the peak width, eventually causing multiple

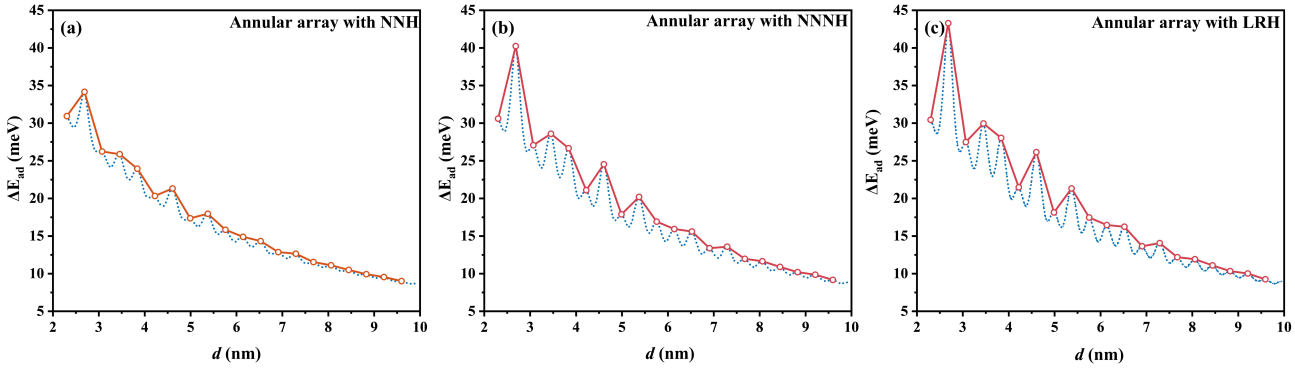

FIG. 10. Dependence of the addition-energy level spacing $\Delta E_{\rm ad}$ (corresponding to the conductance sub-peak spacing) on the nearest-neighbor inter-dopant separation d: (a) NNH model; (b) NNNH model; (c) LRH model.

peaks to overlap and degenerate into conductance envelopes associated with the lower and upper Hubbard bands [20]. Within the resonant tunneling description of electron transport [17], the approximate peak shape corresponding to the n-th conductance peak can be obtained:

$$G_n(\mu) \approx \frac{G_0}{4k_{\rm B}T}\sec^2\left(\frac{\mu - E_{\rm ad}(n)}{2k_{\rm B}T}\right) \tag{46}$$

where G_0 denotes a constant associated with the hopping rate. According to Eq. (46), the maximum value of conductance $G_0/(4k_{\rm B}T)$ is proportional to $1/T$, thereby indicating that the height of the conductance peak decreases inversely with the increase of temperature. Moreover, as follows from the temperature dependence of the full width at half maximum (FWHM) of the conductance peak described by Eq. (44), an increase in temperature gives rise to a progressive broadening of the conductance peak, the ultimate consequence of which is the extensive overlap and effective merging of multiple conductance peaks into an indistinguishable envelope under sufficiently high-temperature conditions. Therefore, the clear experimental observation of quantum phenomena in the dopant-atom quantum-dot array requires the resolvability of the conductance peaks, which demands that the minimum spacing between peak positions, namely, the minimum difference in addition energy, be much greater than FWHM [21]:

$$\min(\Delta E_{\rm ad}) \gg \frac{1}{2}\,\mathrm{FWHM} \approx 1.76k_{\rm B}T \tag{47}$$

The most effective means of enlarging the peak spacing lies in the broadening of the upper and lower Hubbard bands, since such band broadening gives rise to an increase level spacing $\Delta E_{\rm ad}$ in the addition energy spectrum, and hence to a corresponding broadening of the spacing between adjacent conductance sub-peaks. As shown in Fig. 9(b) and (d), the band broadening of NNH, NNNH and LRH models increase successively, accompanied by increases in the spacings between the corresponding conductance sub-peaks to different extents. The origin of such band broadening is attributable to two factors, the coupling strength t, and the nearest-neighbor electronic repulsion energy W. In the interaction-dominated system ($U \gg t$) and under the condition $U \geq 1.345\,W$, the band broadening induced by these two contributions exhibits a linear dependence. In the absence of inter-site electron repulsion, the band broadening Δ is determined entirely by the coupling strength t. Moreover, if the addition energy level spacing $\Delta E_{\rm ad}$ within the same Hubbard subband is assumed to be uniform, one obtains:

$$\Delta = \left(2\sum z_i\right)\cdot t \approx (N-1)\cdot\Delta E_{\rm ad} \tag{48}$$

From Eqs. (47) and (48), it follows that, in the presence of coupling alone, the minimum coupling strength required for the resolution of the conductance peaks satisfies:

$$t \gg \frac{(N-1)}{\sum z_i} \times 1.76k_{\rm B}T \tag{49}$$

For NNH, NNNH and LRH models of 6-site annular array, the minimum coupling strengths required for the resolution of the quantum-conductance peaks at room temperature are $t_{\rm NNH} = 114\,\mathrm{meV}$, $t_{\rm NNNH} = 57.2\,\mathrm{meV}$, $t_{\rm LRH} = 45.76\,\mathrm{meV}$, respectively. However, coupling strengths of this magnitude are unattainable in real physical systems, as already indicated in Fig. 3, thereby necessitating the introduction of inter-site electron repulsion W in order to further enlarge the energy level spacing $\Delta E_{\rm ad}$. Since the increase in band broadening induced by the nearest-neighbor inter-site electron repulsion energy W likewise remains linear, the addition energy level spacing $\Delta E_{\rm ad}$ satisfies the following relationship:

$$\begin{aligned}\Delta &= \left(2\sum z_i\right)\cdot t + \left(\sum_{k=1}^{N-1}\sin\frac{\pi}{N}\csc\frac{k\pi}{N}\right)\cdot W \\ &\approx (N-1)\cdot\Delta E_{\rm ad}.\end{aligned} \tag{50}$$

By combining Eqs (47) and (50), we obtain

$$\begin{aligned}\Delta E_{\rm ad} &\approx \left(\frac{2\sum z_i}{N-1}\right)\cdot t + \frac{\sum_{k=1}^{N-1}\sin\frac{\pi}{N}\csc\frac{k\pi}{N}}{N-1}\cdot W \\ &\gg 1.76k_{\rm B}T.\end{aligned} \tag{51}$$

Therefore, for the preservation of quantum effects at elevated temperatures, the determination of an appropriate inter-dopant separation d_{ij} becomes necessary, such that the band

broadening associated with the coupling strength t and the nearest-neighbor electronic repulsion energy W exceeds the thermal broadening of the conductance peaks induced by temperature. On this basis, we calculated the dependence of the addition energy level spacing ΔE_{ad} on the nearest-neighbor dopant separation d. As shown in Fig. 10, a reduction in the dopant separation leads to an enhanced overlap of the electron wave functions, thereby resulting in an increase in the oscillatory magnitude of the split addition energy level spacing ΔE_{ad}. At room temperature of 300 K, for which $1.76k_{\mathrm{B}}T \approx 45.8$ meV, the required dopant spacing is approximately 2.7 nm, corresponding to a dopant concentration of about $5.2 \times 10^{19}\,\mathrm{cm}^{-3}$.

4. CONCLUSIONS

In this paper, a generalized Fermi-Hubbard model for hydrogenic dopant-atom arrays in silicon is established. By employing the effective Euclidean distance matrix $\boldsymbol{D}$ to characterize the geometric relations among dopant atoms and combining it with the adjacency matrix $\boldsymbol{A}$ to specify the electron-hopping modes within the array, the proposed framework is rendered applicable to the simulation of electron transport in one-dimensional, two-dimensional, and three-dimensional dopant-atom arrays. On the basis of this generalized model, the addition-energy spectrum of the simple two-dimensional annular array with central rotational symmetry is simulated. Through a systematic analysis of the influence of the various energy parameters in the Hubbard Hamiltonian on the band broadening and gap magnitude of the addition energy spectrum, the principal factors governing quantum transport in the Fermi-Hubbard system are identified. The results demonstrate that, in the interaction-dominated system, the band broadening induced by the coupling strength t and the nearest-neighbor inter-site electron repulsion energy W is linear, with proportionality coefficients given respectively by twice the number of hopping paths $2\sum z_i$ and the correlation broadening coefficient β, which depends only on geometric factors. The Coulomb gap magnitude is found to be associated with the critical parameter α corresponding to the reconstruction of the electron configuration. When $U/W > \alpha$ the Coulomb gap is determined solely by the competition between U and t, and exhibits a linear dependence on both parameters in the interaction-dominated system. By contrast, when $U/W < \alpha$, the competition between U and W gives rise to a reconfiguration of the electron arrangement, under which the energy gap becomes jointly dependent on U, t, and W. In addition, the conductance spectrum is calculated based on the addition energy of the array, and the effects of array geometry, electron-hopping mode, energy parameters, and temperature on electron transport are analyzed. The array geometry is shown to exert a direct influence on the Coulomb interaction mediated modulation of electron transport. Under the influence of the inter-site electron repulsion energy W_{ij}, transport in the one-dimensional array is significantly suppressed, whereas that in the two-dimensional array is comparatively less affected, owing to the non-collinearity between the direction of electron transport and that of the inter-site electronic repulsion. The electron-hopping modes within the array exert a pronounced influence on transport behavior, which is manifested in the conductance differences among different hopping modes: an increase in the number of available hopping paths corresponds to an increase in the complexity of the hopping dynamics, an increase in the number of nonzero transition-matrix elements, and consequently an increase in the average conductance. On the one hand, the positions of the conductance peaks are determined by the on-site electron repulsion energy U, the nearest-neighbor electron repulsion energy W, and the coupling strength t. On the other hand, the nearest-neighbor electron repulsion energy W and the coupling strength t further govern the distribution of peak heights through their modulation of the electron hopping probability, thereby leading to distinct conductance-envelope shapes in different systems. The influence of temperature on the conductance spectrum is manifested primarily in the suppression of the peak conductance and the broadening of the full width at half maximum, with the latter giving rise to the overlap of multiple conductance peaks, and hence to the loss of peak resolvability. Therefore, the maintenance of observable quantum effects at elevated temperatures necessitates the selection of an appropriate inter-dopant separation, so that the thermally induced broadening does not compromise the required separation between conductance peaks.

The generalized Fermi–Hubbard model for hydrogenic dopant-atom arrays in silicon can serve not only as a theoretical framework for investigating the underlying physical mechanisms of novel strongly correlated quantum phenomena in Fermi–Hubbard systems, including strong-correlation effects, the Anderson–Mott transition, and unconventional superconductivity, but also as an effective tool for elucidating the complex many-body electron-correlation effects in silicon transistors. Accordingly, this work provides a theoretical basis for the design and development of dopant-atom transistors and their arrays based on hydrogenic dopant-atom manipulation, and is expected to offer valuable guidance for the realization and regulation of strongly correlated quantum functional devices in silicon-based platforms.

DATA AVAILABILITY

The linked data associated with this paper can be accessed through the Scientific Data Bank: https://doi.org/10.57760/sciencedb.j00213.00184.

ACKNOWLEDGMENTS

This work was supported by the National Natural Science Foundation of China (Grant No. 62374157).

REFERENCES

[1] E. Prati, M. Hori, F. Guagliardo, G. Ferrari, and T. Shinada, Nat. Nanotechnol. **7**, 443 (2012).

[2] X. Q. Wang, E. Khatami, F. Fei, J. Wyrick, P. Namboodiri, R. Kashid, A. F. Rigosi, G. Bryant, and R. Silver, Nat. Commun. **13**, 6824 (2022).
[3] J. Hubbard, Proc. R. Soc. London A **276**, 238 (1963).
[4] C. W. J. Beenakker, Phys. Rev. B **44**, 1646 (1991).
[5] G. Chen, G. Klimeck, S. Datta, G. Chen, and W. A. Goddard, Phys. Rev. B **50**, 8035 (1994).
[6] Z. M. Yu, A. T. Johnson, and T. Heinzel, Phys. Rev. B **58**, 13830 (1998).
[7] N. H. Le, A. J. Fisher, and E. Ginossar, Phys. Rev. B **96**, 245406 (2017).
[8] S. S. Wang, K. Li, Y. M. Dai, H. H. Wang, Y. C. Zhang, and Y. Y. Zhang, Sci. Rep. **13**, 5763 (2023).
[9] S. Devi, P. K. Ahluwalia, and S. Chand, Pramana **94**, 60 (2020).
[10] J. K. Gamble, N. T. Jacobson, E. Nielsen, A. D. Baczewski, J. E. Moussa, I. Montaño, and R. P. Muller, Phys. Rev. B **91**, 235318 (2015).
[11] X. Hu, B. Koiller, and S. Das Sarma, Phys. Rev. B **71**, 235332 (2005).
[12] B. Weber, S. Mahapatra, H. Ryu, S. Lee, A. Fuhrer, T. C. G. Reusch, D. L. Thompson, W. C. T. Lee, G. Klimeck, L. C. L. Hollenberg, and M. Y. Simmons, Science **335**, 64 (2012).
[13] B. Voisin, J. Bocquel, A. Tankasala, M. Usman, J. Salfi, R. Rahman, M. Simmons, L. Hollenberg, and S. Rogge, Nat. Commun. **11**, 6124 (2020).
[14] J. C. Slater and G. F. Koster, Phys. Rev. **94**, 1498 (1954).
[15] P. R. Grzybowski and R. W. Chhajlany, Phys. Status Solidi B **249**, 2231 (2012).
[16] E. Janod, J. Tranchant, B. Corraze, M. Querré, P. Stoliar, M. Rozenberg, T. Cren, D. Roditchev, V. T. Phuoc, and M. P. Besland, Adv. Funct. Mater. **25**, 6287 (2015).
[17] N. Y. Morgan, D. Abusch-Magder, M. A. Kastner, Y. Takahashi, H. Tamura, and K. Murase, J. Appl. Phys. **89**, 410 (2001).
[18] M. H. Cha and J. Hwang, Sci. Rep. **10**, 16701 (2020).
[19] M. A. Ochoa, K. Liu, M. Zieliński, and G. Bryant, Phys. Rev. B **109**, 205412 (2024).
[20] D. Gerace, E. Pavarini, and L. C. Andreani, Phys. Rev. B **65**, 155331 (2002).
[21] K. S. Yi, K. Trivedi, H. C. Floresca, H. Yuk, W. Hu, and M. J. Kim, Nano Lett. **11**, 5465 (2011).